Truncation correction for oblique filtering lines

Stefan Hoppe[a] and Joachim Hornegger[b]
Institute of Pattern Recognition, University of Erlangen-Nuremberg, Erlangen, Bavaria 91058, Germany

Günter Lauritsch[c] and Frank Dennerlein[d]
Siemens AG, Healthcare Sector, Forchheim 91301, Germany

Frédéric Noo[e]
UCAIR, Department of Radiology, University of Utah, Salt Lake City, Utah 84108

(Received 24 June 2008; revised 2 September 2008; accepted for publication 23 September 2008; published 24 November 2008)

State-of-the-art filtered backprojection (FBP) algorithms often define the filtering operation to be performed along oblique filtering lines in the detector. A limited scan field of view leads to the truncation of those filtering lines, which causes artifacts in the final reconstructed volume. In contrast to the case where filtering is performed solely along the detector rows, no methods are available for the case of oblique filtering lines. In this work, the authors present two novel truncation correction methods which effectively handle data truncation in this case. Method 1 (basic approach) handles data truncation in two successive preprocessing steps by applying a hybrid data extrapolation method, which is a combination of a water cylinder extrapolation and a Gaussian extrapolation. It is independent of any specific reconstruction algorithm. Method 2 (kink approach) uses similar concepts for data extrapolation as the basic approach but needs to be integrated into the reconstruction algorithm. Experiments are presented from simulated data of the FORBILD head phantom, acquired along a partial-circle-plus-arc trajectory. The theoretically exact M-line algorithm is used for reconstruction. Although the discussion is focused on theoretically exact algorithms, the proposed truncation correction methods can be applied to any FBP algorithm that exposes oblique filtering lines. © *2008 American Association of Physicists in Medicine*.
[DOI: 10.1118/1.3002416]

Key words: truncation correction, cone-beam reconstruction, computed tomography

I. INTRODUCTION

Computed tomography (CT) imaging with C-arm systems has become an important tool in interventional radiology for treatment assistance and assessment of treatment success in specific regions-of-interest (ROI), such as the liver, the heart, the head, or a section of the spine. To achieve 3D reconstruction of the ROI, data acquisition is typically performed with a cone beam (CB) of x-rays focused on the ROI, while the source-detector assembly follows a specified path around the patient. Currently, the preferred path is a simple circular short-scan motion. But more sophisticated motions are also possible, such as a partial-circle-plus-arc motion,[1] and are likely to become the method of choice in the future, as they provide data allowing more accurate reconstructions.

For reconstruction, a filtered-backprojection (FBP) method is generally used. Such methods have been developed not only for the circular short-scan trajectory,[2,3] but also for the partial-circle-plus-arc trajectory.[4,5] As indicated by their name, FBP methods perform reconstruction of the ROI by first filtering the projections, then backprojecting the filtered projections. A certain amount of data is needed for reconstruction at any given location $\underline{x}_0$ inside the ROI. First, the backprojection must be achievable. For this to be the case, the line that connects the source position to $\underline{x}_0$ must hit the detector for all source-detector positions required for reconstruction at $\underline{x}_0$, as dictated by the reconstruction algorithm. This condition defines a minimum data requirement that we will assume to be always satisfied; it basically states that there is enough data to perform reconstruction if the object was reduced to a tiny sphere centered at $\underline{x}_0$. Second, the detector must be large enough to encompass at each source position the data required for application of the filtering step. This second condition is often violated in practice, because the size of the flat-panel detector is fairly limited (on most systems, the detector size is only 30×40 cm^2). When the second condition is violated for a source position that is required for reconstruction at $\underline{x}_0$, we say that the associated projection is truncated.

To mitigate artifacts due to truncation, data extrapolation techniques are needed. Such techniques have been developed for conventional circular short-scan FDK reconstruction,[2,6] which involves only filtering along the detector rows. However, new circular short-scan reconstruction methods, such as the ACE method,[3] involve filtering on lines that are not oriented along the detector rows (or columns), and so do reconstruction algorithms designed for partial-circle-plus-arc data acquisition. Thus, there is a need to develop accurate extrapolation techniques for handling filtering along oblique lines in the presence of truncation. This paper suggests two solutions dedicated to this need: one totally general solution (basic approach) and one algorithm-specific solution (kink approach). Our work builds on techniques used for handling truncation along detector rows. Such techniques have been

intensively discussed in the literature. In 2000, Ohnesorge *et al.*[7] proposed a method where the truncated data are extrapolated by a data mirroring operation at the truncated detector border. In 2002, Ruchala *et al.*[8] merged *a priori* information retrieved from planning CT data with the acquired projection images to estimate the missing data. In 2004, Hsieh *et al.*[9] developed a method that extrapolates the data by assuming that the projection values of the missing portion of the object are generated by x-rays which travel through a water cylinder. In 2005, Zellerhoff *et al.*[10] presented a hybrid method, which is a combination of the water cylinder approach of Hsieh and a Gaussian data extrapolation. In 2007, Zamyatin and Nakanishi[11] proposed a method to handle data truncation in the fan-beam and cone-beam case by extrapolating along the sinogram curve of each reconstruction point.

In this paper, we focus on the partial-circle-plus-arc trajectory, which can be easily performed with a C-arm system. We apply the M-line reconstruction algorithm, originally presented by Pack and Noo,[5] and we build our truncation correction methods on the approach of Zellerhoff. This approach was preferred because it seemed most amenable to our problem, while being routinely used in the clinical environment. Under these settings, our results show that truncation artifacts resulting from oblique lines can be dramatically reduced and sometimes even be virtually eliminated. The level of performance depends on the data truncation geometry (and also, of course, on the imaged object itself). Also, we will see that both proposed truncation correction methods perform very similarly, so that the selection of one method versus the other should be primarily based on the specifics of the data acquisition geometry and ease of fitting within the data-processing pipeline.

The paper is organized as follows. In Sec. II, we review the reconstruction steps of the M-line algorithm with a special focus on the filtering operation to define the problem of data truncation. Section III introduces our new methods. Experiments are presented in Sec. IV for simulated cone-beam data. Section V summarizes our results.

II. BACKGROUND

In this section, we first review the steps of the M-line reconstruction algorithm of Pack and Noo[5] in the specific context of reconstruction from a partial-circle-plus-arc trajectory. Then, we define how truncation affects this partial-circle-plus-arc algorithm.

II.A. M-line reconstruction algorithm

The M-line reconstruction algorithm was invented in 2005 by Pack and Noo[5] as a theoretically exact image reconstruction method. In general, this reconstruction formula can be applied on any complete source trajectory according to the definition given by Tuy.[12] However, the following algorithmic steps are specific to its application on the partial-circle-plus-arc trajectory. Figure 1 explains the fundamental setup for a better understanding of those steps. As can be seen in this figure, the method involves a specific point, called M-point, on the source trajectory. In general, this point

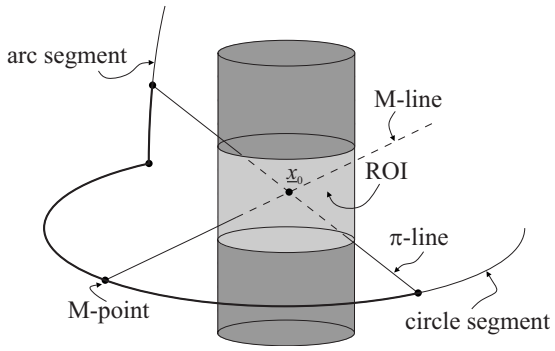

FIG. 1. M-line reconstruction for the partial-circle-plus-arc trajectory. For each location $\underline{x}_0$ inside the ROI, there is one associated M-line and one associated π-line. The M-line defines the filtering directions for $\underline{x}_0$. The π-line delimitates the portion of the trajectory (shown in dark) from where the data must be backprojected onto $\underline{x}_0$ to perform a theoretically exact reconstruction at $\underline{x}_0$.

can depend on the location $\underline{x}_0$ in the ROI, but at a cost in efficiency. For our purposes, we assume the M-point is chosen independently of $\underline{x}_0$. That means that all reconstruction points are associated to the same M-point; this M-point is located on the partial-circle scan, as indicated in the figure.

M-line image reconstruction of a region-of-interest involves the following steps:

(1) **View differentiation**. Differentiate the cone-beam projections with respect to the source trajectory parameter (typically the rotation angle of the source-detector assembly) at fixed ray direction. Picture the outcome as a new set of projections, each associated with one source position.
(2) **Cosine weighting**. Weight each detector pixel value to equalize the distance between the detector pixel and the focal spot.
(3) **Forward rebinning**. For each source position, interpolate the detector pixel values to create values on a set of oblique lines, as depicted in Fig. 2. View the values on each oblique line as one row of a new, rebinned detector grid. The oblique lines are generally called the filtering lines; they are the projections of the M-lines onto the detector plane (cf. Fig. 1), and they thus all intersect at

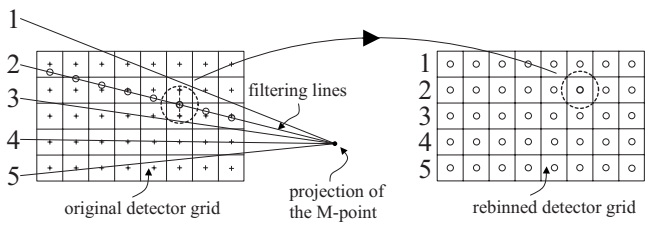

FIG. 2. Forward rebinning: the values on the rebinned detector grid (right) are generated by linear interpolation from the values on the original detector grid (left). The filtering lines are sampled such that interpolation needs to be done only in vertical direction. In horizontal direction, both detector grids coincide. The figure shows a case with five filtering lines. As illustrated, the detector values that are at the two positions (crosses "+") within the dashed circle on the left are interpolated to produce the rebinned detector value within the dashed circle on the right.

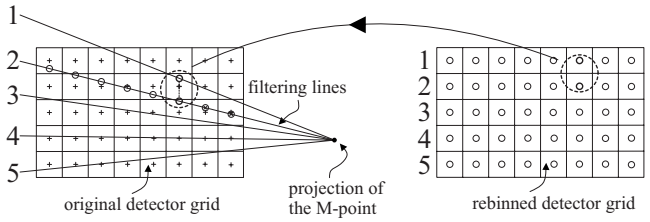

FIG. 3. Backward rebinning: the values on the original detector grid (left) are generated by linear interpolation from the values on the rebinned detector grid (right), similar to the forward rebinning case. The figure shows a case with five filtering lines. As illustrated, the rebinned detector values that are at the two positions (circles "o") within the dashed circle on the right are interpolated to produce the detector value within the dashed circle on the left.

the same point, namely the projection of the M-point.

(4) **Hilbert filtering**. For each source position, apply a one-dimensional Hilbert transform along the filtering lines, i.e., along the rows of the rebinned detector grid.
(5) **Backward rebinning**. For each source position, generate values on the original detector grid by interpolation of the values from the rebinned detector grid, as depicted in Fig. 3.
(6) **Data selection**. Identify the backprojection range for each point $\underline{x}_0$ in the ROI. This range corresponds to the curve that is bounded by the endpoints of the π-line through $\underline{x}_0$; see Fig. 1.
(7) **Backprojection**. Backproject the filtered data that results from step 5, involving for each point $\underline{x}_0$ only the source positions that have been identified in step 6.

II.B. Data truncation

Assume steps 1–3 of the M-line algorithm (see above) have already been applied on the cone-beam data and let $g(s)$ denote the output of step 3. Consequently, $g(s)$ represents the (differentiated and cosine weighted) cone-beam values along a given filtering line. Step 4 of the M-line algorithm amounts to the computation of the filtered data

$$g_F(s) = \int_{-\infty}^{+\infty} h_{\text{Hilb}}(s-s')g(s')ds' . \tag{1}$$

In this equation, $h_{\text{Hilb}}(s)$ is the Hilbert kernel in the spatial domain

$$h_{\text{Hilb}}(s) = \frac{1}{\pi s} . \tag{2}$$

Since $h_{\text{Hilb}}(s)$ has infinite support, the filtering operation involves all values of $g(s)$ along the line. In case of data truncation, only a subset of the values on this line will be available. Therefore, the filtering operation has to be performed without having all values along the line. This causes truncation artifacts in the final reconstructed image (Sec. IV demonstrates the effect). The truncation process can be seen as a multiplication of $g(s)$ with a rectangular window, which cuts out a certain portion of the values along the filtering line, before the computation of the integral in (1) is performed.

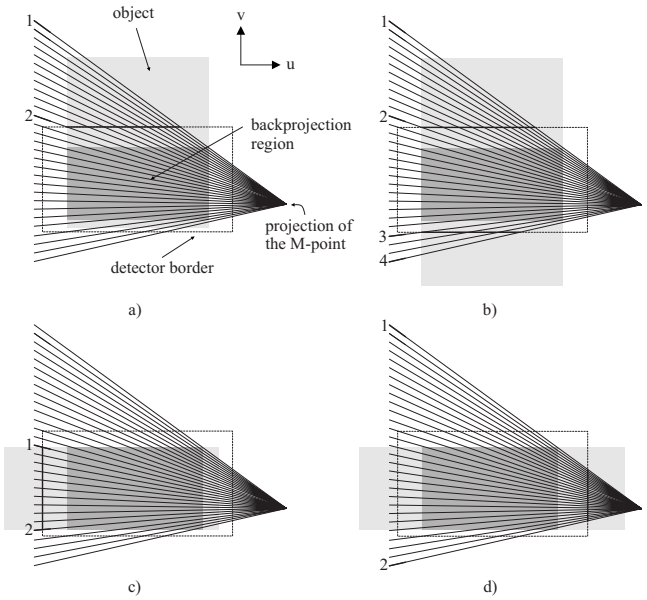

FIG. 4. Filtering line truncation for the M-line algorithm where all filtering lines intersect in a single point. (a) The filtering lines between 1-2, (b) between 1-2 and 3-4, (c) between 1-2, and (d) between 1-2 are truncated. Arbitrary combinations are possible.

The multiplication of $g(s)$ with a rectangular window in the spatial domain corresponds to a convolution of $g(s)$ with a sinc function in the frequency domain, and this convolution smears the spectrum of $g_F(s)$.

We may define data truncation as follows: *Any filtering line that leaves the detector before it leaves the shadow of the object is a truncated filtering line and leads to reconstruction artifacts for each point which projects onto it.*

Figure 4 displays several scenarios for a set of possible filtering lines for the M-line algorithm. Depending on the location of the M-point and on the projection under consideration, the M-point will project inside or outside of the detector. For the rest of the paper, we assume that it projects outside of the detector as in the figure, which will be the case when the M-point is placed approximately in the middle of the partial-circle segment of the partial-circle-plus-arc trajectory, at least for a typical C-arm geometry; see also Ref. 13. We further discuss this in Sec. V. Note that only points within the backprojection region (the detector area depicting the ROI) need to be filtered.

III. TRUNCATION CORRECTION

Both proposed truncation correction methods build upon the so-called water cylinder correction originally presented by Hsieh *et al.*[9] in combination with a Gaussian extrapolation shown by Zellerhoff *et al.*[10] Those methods will therefore be reviewed briefly before presenting the new material.

III.A. Review: Water cylinder correction

In 2004, Hsieh *et al.*[9] investigated the problem of truncation for the FDK reconstruction for data on a circular scan. He presented a truncation correction method that handles

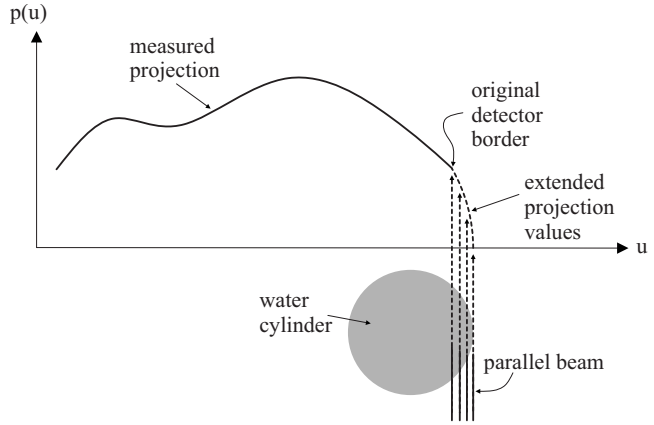

FIG. 5. Water cylinder correction: the projection values $p(u)$ along one detector row are truncated at the right detector border. For each detector row and for each side of that row, the extent (midpoint and radius) of a 2D water cylinder is determined and the missing portion of the object is approximated by integrals along parallel rays through that cylinder; see Ref. 9 for details.

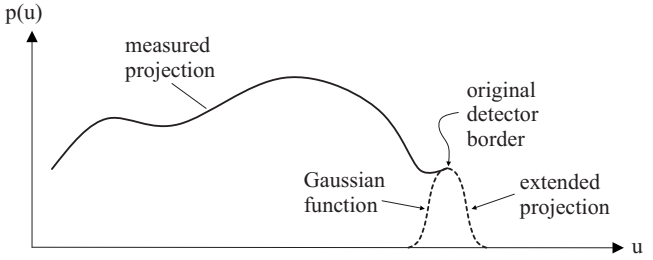

FIG. 6. Gaussian extrapolation: the projection values at the truncated detector boundary increase. In this case, a Gaussian function is fit to the data; see Ref. 10 for details.

truncation along the detector rows, along which the ramp filtering is applied. In this method, all detector rows are regarded independently of one another. The projection values along each row are treated as if they were measurements taken along parallel rays in a 2D plane. By doing so, the method ignores the cone angle and the fan angle of the cone-beam. In case of data truncation, the method approximates the missing measurements by integrals along parallel rays through a 2D water cylinder. The extent (midpoint and radius) of the cylinder is determined to achieve continuous data up to the second order; see Fig. 5.

The method produces decreasing projection values for the missing part of the object, if the measured values decrease towards the detector boundary because then the midpoint of the water cylinder will be fitted on the "measured side" of the boundary as in the figure. Otherwise, if the projection values increase towards the detector boundary, the midpoint of the water cylinder will be fitted on the "unmeasured side" of the boundary and so the extrapolated projection values will first increase before they decrease again.

III.B. Review: Hybrid approach

In 2005, Zellerhoff *et al.*[10] refined the water cylinder correction to differently handle the case when the midpoint of the water cylinder is fitted on the "unmeasured side" of the boundary (see discussion above). They found on real data that in this case, better results can be achieved if the water cylinder fit is replaced by a Gaussian extrapolation. To perform this extrapolation, the center and the standard deviation of the Gaussian need to be determined. The center of the Gaussian is set to the location of the last available projection value; see Fig. 6. For the computation of the standard deviation, the method assumes that this last projection value, say $p(u_0)$, corresponds to an integral along a ray through a water-equivalent object (with attenuation coefficient μ_W). The ray's intersection length l with this object is then defined by $l = p(u_0)/\mu_W$, and the standard deviation of the Gaussian is set to 25% of l.

The method always produces decreasing projection values for the missing part of the object although in the case of a Gaussian fit, the extrapolated data are continuous only up to the first order. For future reference, this combination of water cylinder correction and Gaussian extrapolation will be called the hybrid approach.

III.C. Preliminary considerations

A straightforward data truncation correction method for oblique filtering lines would apply the hybrid approach along the filtering lines themselves instead of applying it along the detector rows as in Ref. 10. However, Zellerhoff designed this approach primarily as a data truncation correction method that is applied to the FDK algorithm. The FDK algorithm does not incorporate the view dependent data differentiation step, which is inherent to the M-line algorithm. This data differentiation step is crucial since the nature of the differentiated cone-beam data is very different from that of the original, nondifferentiated cone-beam data. Because the hybrid approach was designed to operate on nondifferentiated cone-beam data, there is no justification for applying it after the data differentiation step. In particular, the values on the filtering lines correspond to differentiated cone-beam data. Therefore, this straightforward data truncation method does not seem reasonable. With this in mind, we designed two alternative approaches that avoid this difficulty. Those methods are presented hereafter.

III.D. Method 1: Basic approach

The basic approach (BA) makes use of the hybrid approach in two data preprocessing steps. In step 1 (BA-R), the hybrid approach is applied along the detector rows. In step 2 (BA-C), the hybrid approach is applied again, this time along the detector columns of the extended detector rows. After those two steps, the reconstruction algorithm is used without modification. The extended reconstruction algorithm comprises the following steps:

(1) **BA-R**. Apply the hybrid approach along the detector rows.

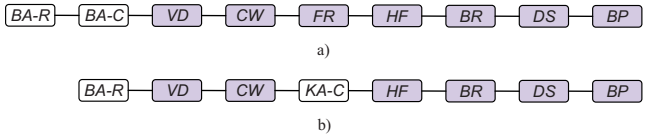

FIG. 7. Proposed truncation correction methods in block diagram format. Shaded boxes correspond to the conventional steps of the M-line algorithm, white boxes correspond to the proposed truncation correction steps. (a) Basic approach (BA-R, BA-C). (b) Kink approach (BA-R, KA-C). The remaining block labels are as follows: view differentiation (VD), cosine weighting (CW), forward rebinning (FR), Hilbert filtering (HF), backward rebinning (BR), data selection (DS), and backprojection (BP).

(2) **BA-C**. Apply the hybrid approach along the detector columns.
(3) **View differentiation**.
(4) **Cosine weighting**.
(5) **Forward rebinning**.
(6) **Hilbert filtering**.
(7) **Backward rebinning**.
(8) **Data selection**.
(9) **Backprojection**.

Figure 7(a) shows the complete algorithm in block diagram format.

III.E. Method 2: Kink approach for the partial-circle-plus-arc geometry

While the basic approach makes no assumptions about the specific geometry, the kink approach is designed for the partial-circle-plus-arc trajectory and relies on the fact that one detector axis is always aligned almost parallel to the plane of the partial-circle scan and that the M-lines tend to be less oblique relative to this axis. This axis defines our detector rows. The axis orthogonal to the rows then defines the detector columns; see Fig. 8.

As with the basic approach, the kink approach (KA) consists of two steps. Step 1 is identical to the first step of the basic approach, BA-R, i.e., the hybrid approach is applied

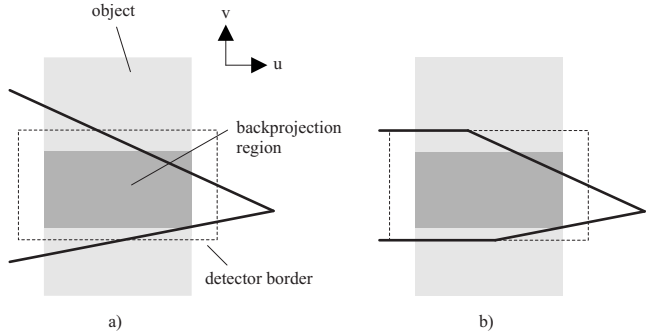

FIG. 9. Method 2: the Kink Approach. Filtering is done along lines with a kink if these lines exceed the detector in the direction of the detector columns. (a) Original filtering lines. (b) Corresponding filtering lines with kink. The setup matches that of Fig. 4(b). Note that the backprojection region could become as large as the detector.

along the detector rows. In contrast to the basic approach, step 2 (KA-C) modifies the filtering lines if these lines exceed the detector in the direction of the detector columns such that in this case, filtering is done along lines with a kink; see Fig. 9. When a line intersects the detector border, the samples are taken from the first or last detector row, respectively. This can be efficiently incorporated into a modified forward rebinning step.

Compared to the basic approach, the kink approach does not require extension of the detector in both directions. This allows some savings in data storage and may facilitate a hardware implementation. The kink approach may be seen as an application of the "row repetition" technique[14] that is widely used by CT manufacturers for data extrapolation with no additional data storage requirement.

The extended reconstruction algorithm comprises the following steps:

(1) **BA-R**. Apply the hybrid approach along the detector rows.
(2) **View differentiation**.
(3) **Cosine Weighting**.

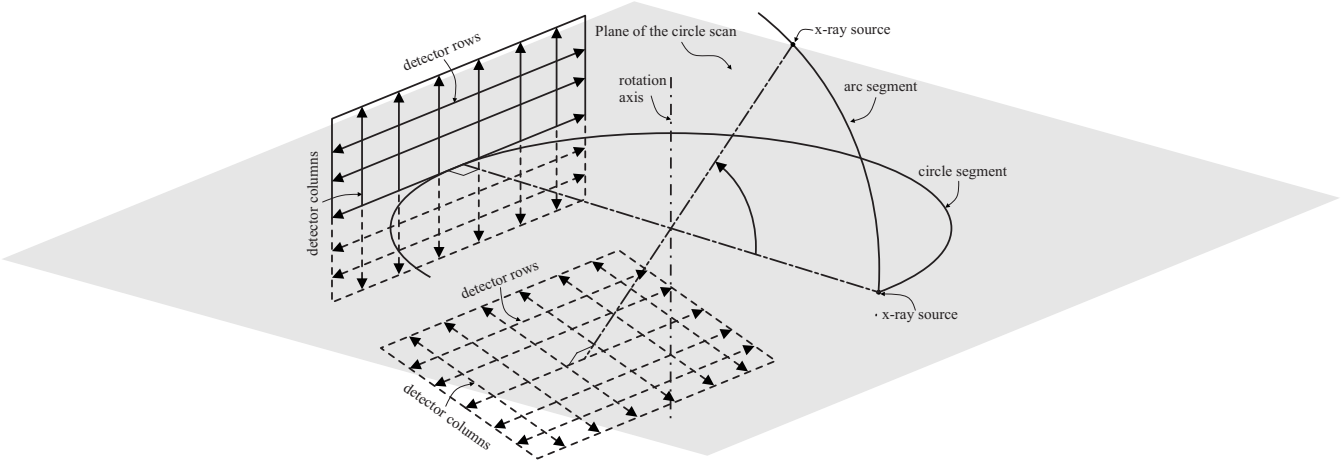

FIG. 8. Geometrical setup of the detector relative to the partial-circle-plus-arc trajectory. Whether the x-ray source moves along the partial-circle or along the arc segment, one axis (the one defining the orientation of the detector rows) is always aligned almost parallel to the plane of the partial-circle scan.

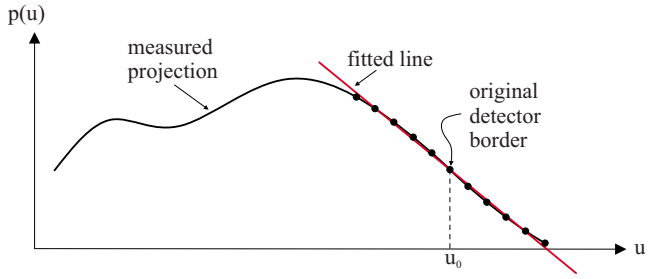

FIG. 10. The value of $p'(u_0)$ is approximated by the slope of the line closest to the projection values $p(u_{-K}),\ldots,p(u_K)$. For that visualization, we used $K=5$.

(4) **KA-C**. Perform a modified forward rebinning from detector coordinates to filtering line coordinates by taking the samples from the first or last detector row if a filtering line exceeds the detector in the direction of the detector columns.
(5) **Hilbert filtering**.
(6) **Backward rebinning**.
(7) **Data selection**.
(8) **Backprojection**.

Figure 9(b) shows the complete algorithm in block diagram format.

III.F. Measurement noise

In a realistic scenario, the projection values will be disturbed by measurement noise. A stable and robust implementation of the proposed methods must consider fluctuations in the projection values caused by noise. In fact, there is one implementation step, common to both proposed methods, which may become critical in the presence of measurement noise. This step is part of the original water cylinder correction, which in turn is part of the hybrid approach on which our methods are built. Specifically, the water cylinder correction requires the computation of the derivative $p'(u_0)$ of the projection curve at the location u_0 of the last available projection value. To achieve a robust implementation, we use techniques similar to those suggested by Hsieh *et al.*[9] That is, we compute $p'(u_0)$ by fitting a line to a set of projection values $p(u_i)$, with $i=-K,\ldots,0,\ldots,K$, $K\in\mathbb{N}$. The slope of the fitted line is then taken as an approximation for $p'(u_0)$. The values $p(u_{-K}),\ldots,p(u_{-1})$ as well as the last available projection value $p(u_0)$ are measured values. The values $p(u_1),\ldots,p(u_K)$ are generated from $p(u_{-K}),\ldots,p(u_{-1})$ by an antisymmetric mirroring operation, according to

$$p(u_k)=2p(u_0)-p(u_{-k}) \tag{3}$$

with $k=1,\ldots,K$; see Fig. 10. Given the pairs $(p(u_i),u_i)$, we set up the following linear system of equations

$$A\underline{l}=\underline{0} \tag{4}$$

where

$$A=\begin{bmatrix} p(u_{-K}) & u_{-K} & 1 \\ & \vdots & \\ p(u_0) & u_0 & 1 \\ & \vdots & \\ p(u_K) & u_K & 1 \end{bmatrix} \tag{5}$$

is the $(2K+1)\times 3$ measurement matrix and $\underline{l}=(l_1,l_2,l_3)^{\mathsf{T}}$ is the representation of the line in homogeneous coordinates. For a unique solution to exist, it is required that A has at least dimension 2×3. However, for improved stability, we use $K=12$, resulting in a measurement matrix A of dimension 25×3, and we define the solution l as the vector of norm 1 that minimizes $\|A\underline{l}\|$. Numerically, this solution can be calculated as the right-hand singular vector corresponding to the smallest singular value of A by using a singular value decomposition. This basically corresponds to a linear least-squares estimation of $\underline{l}$. After solving for $\underline{l}$, $p'(u_0)=-l_1/l_2$. The sign of $p'(u_0)$ is used in the hybrid approach, to decide whether the water cylinder correction or the Gaussian extrapolation must be applied.

IV. EXPERIMENTS AND RESULTS

In this section we present a performance evaluation of our proposed truncation correction methods. We first explain the general experimental setup and provide the involved parameter settings. We then define a figure of merit, which is used to compute the degree of data truncation. Finally, the truncation correction performance is evaluated quantitatively and qualitatively.

IV.A. General setup

We have evaluated the basic approach and the kink approach on simulated cone-beam data of the FORBILD head phantom. The simulation was done by using a partial-circle-plus-arc (or more precisely a short-scan-plus-arc) trajectory with parameter settings that are typical of a commercial C-arm system. The radius of both, partial-circle as well as arc segment of the trajectory, was set to 750 mm while the source-to-detector distance was set to 1200 mm. The detector was simulated with 1024^2 square pixels of side length 0.4 mm. The sampling rate was 0.4°/projection, resulting in 500 (=199.6°) projections for the partial-circle scan and 58 (=22.8°) projections for the arc scan. The arc scan was positioned at the start of the partial-circle scan. For reconstruction, the M-line algorithm was used. The M-point was positioned at 140° on the partial-circle scan, measured from the start of the arc segment. In general, it is preferred to position the M-point at the middle of the partial-circle scan to produce less oblique filtering lines. Here, we explicitly selected the M-point differently to accentuate the obliqueness of filtering lines and thus truncation problems.

For our evaluation, we designed three experiments that differ from each other by the type of data truncation. We distinguish between trans-axial, axial, and combined data truncation. For the trans-axial data truncation experiment, we truncated the cone-beam data by cutting off a specific num-

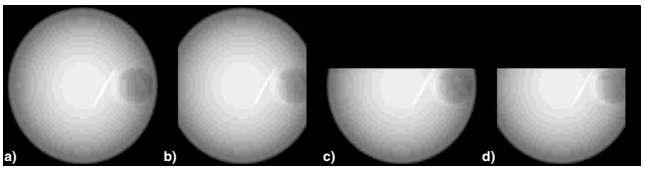

FIG. 11. Artificial truncation, shown exemplarily for the first projection of the partial-circle scan for the FORBILD head phantom. (a) Original projection, no data truncation. (b) Trans-axial data truncation with 100 detector columns on both sides cut off. (c) Axial data truncation with 400 top detector rows cut off. (d) Combined data truncation as a combination of (b) and (c).

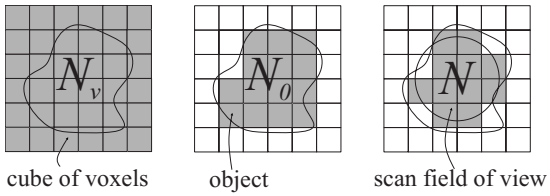

FIG. 12. The quantities N_v, N_0, and N count the number of dark voxels. For N_0 and N, the decision if a voxel is counted or not is based on the location of the voxel's midpoint. For display reasons, this example is in 2D but the same principle is applied in 3D. Note that the scan field of view does not have to be circular as depicted.

ber of detector columns. For the axial data truncation experiment, we cut off a specific number of detector rows instead. The combined data truncation experiment represents a combination of both, the trans-axial and the axial data truncation experiments.

For each experiment, we tested 11 levels of data truncation. The first level corresponds to zero truncation while the last level corresponds to the maximal degree of truncation. For trans-axial data truncation, two successive levels differ by a truncated area of 10 detector columns on each side of the projection image. The maximal cutoff is 100 detector columns. For axial data truncation, two successive levels differ by a truncated area of 40 detector rows, measured from the top of the projection image. The maximal cutoff is 400 detector rows. For combined data truncation, two successive levels differ by a truncated area of 10 detector columns and 40 detector rows. The maximal cutoff is 100 detector columns and 400 detector rows. The columns were cut off from both sides of the projection image and the rows from the top of the projection image, as before. Figure 11 shows example projection images with trans-axial, axial, and combined data truncation.

We have organized the evaluation as follows. For each experiment, we first provide quantitative truncation correction performance results. Then, we show qualitatively the visual image quality that can be achieved with our methods. For the reconstructed volumes of the quantitative evaluation, we chose a coarse Cartesian grid of 256^3 cubic voxels of side length 1.0 mm. For the visual image quality, we refined the grid and used 512^3 voxels of side length 0.5 mm instead. In any case, the volumes always contain the whole object.

IV.B. Scan field of view

For the computation of the degree of truncation (see next section), it is important to first compute the scan field of view. We define this field of view as the union of voxels that are located where the M-line reconstruction would be possible if the Hilbert filtering step was not part of the algorithm. To determine the size and shape of the scan field of view, we start with a large volume of voxels and then eliminate in a loop over the projections each of the voxels of this volume that is spurious. A voxel is eliminated when the projection of its center (say $\underline{x}_0$) onto the detector plane falls outside the detector while the source position is on the trajectory segment required for reconstruction at $\underline{x}_0$; see Fig. 1. In other words, if the projection of a voxel falls outside the detector only for source positions that are not involved in the backprojection step for reconstruction at this voxel, then the voxel belongs to the scan field of view. The scan field of view corresponds to the region where the minimum data requirement mentioned in the Introduction is fulfilled.

IV.C. Degree of truncation

To quantitatively show how much data truncation our three experiments involve, we use a figure of merit called DoT (degree of truncation):

$$\mathrm{DoT} = 1 - N/N_0, \tag{6}$$

where N and N_0 are defined as follows. Consider a Cartesian grid of voxels that encompasses the object to be reconstructed, and let N_v be the number of voxels in this grid. Parameter $N_0 < N_v$ is the number of voxels that are inside the object, while parameter $N < N_0 < N_v$ is the number of voxels that are inside the object as well as inside the scan field-of-view. Obviously, the value of N depends on the detector size. Basically, DoT quantifies how much of the object is affected by truncation for implementation of the backprojection step alone. If $N = N_0$, no portion of the object is affected by truncation and so DoT = 0. On the other hand, if $N = 0$, the whole object is truncated and so DoT = 1. Figure 12 displays N_v, N_0, and N. To compute the DoT, the extent of the reconstructed object must be known or at least be estimated. Figures 13–15

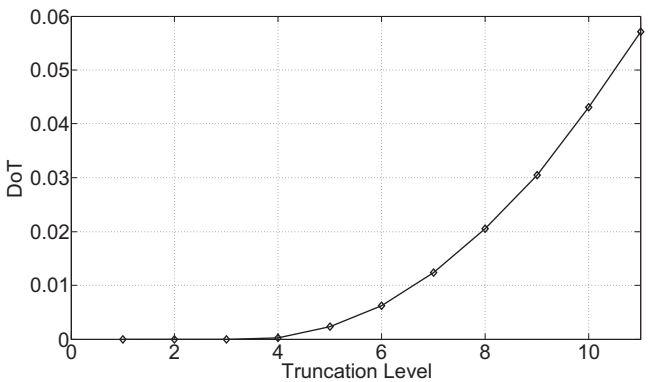

FIG. 13. DoT for trans-axial data truncation. The first truncation level corresponds to zero truncation while the last truncation level corresponds to the maximal truncation (DoT = 5.7%), where 100 detector columns have been cut off on both sides of the projection image.

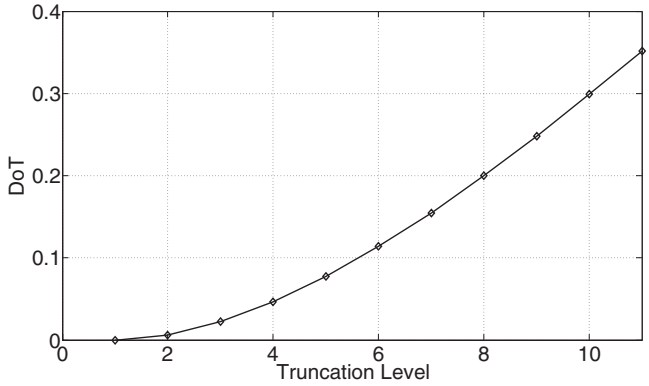

FIG. 14. DoT for axial data truncation. The first truncation level corresponds to zero truncation while the last truncation level corresponds to the maximal truncation (DoT=35.2%), where 400 detector rows have been cut off from the top of the projection image.

show the DoT for each of our three experiments, as a function of the truncation level.

IV.D. Truncation correction performance

To measure the average voxel error for the basic approach and the kink approach, we define the root mean square (RMS) error σ between the reconstructed object without data truncation V^* and the reconstructed object with a specific degree of data truncation V according to

$$\sigma = \left(\frac{1}{N} \sum_{i=1}^{N} (V^*(\underline{x}_i) - V(\underline{x}_i))^2 \right)^{1/2}, \tag{7}$$

where the $\underline{x}_i$'s denote only voxels that have their midpoint inside the reconstructed object as well as inside the scan field of view. The parameter N counts the number of those voxels, as in the DoT formula (6). From one truncation level to the next, the scan field of view decreases and, thus, the parameter N also decreases. We computed the RMS error for the trans-axial, the axial, and the combined data truncation experiments. The resulting curves are shown in Figs. 16–18.

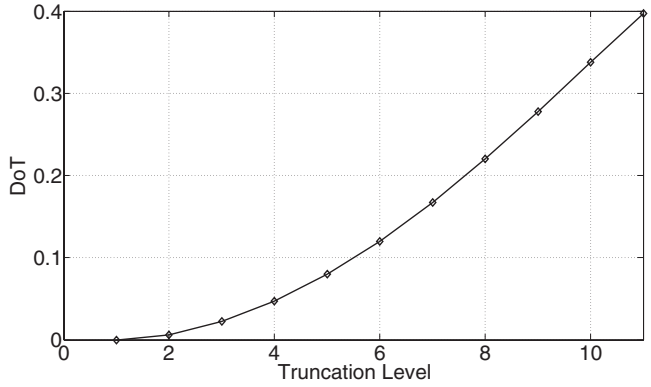

FIG. 15. DoT for combined data truncation. The first truncation level corresponds to zero truncation while the last truncation level corresponds to the maximal truncation (DoT=39.7%), where 100 detector columns and 400 detector rows have been cut off. The columns have been cut off on both sides of the projection image and the rows have been cut off from the top of the projection image.

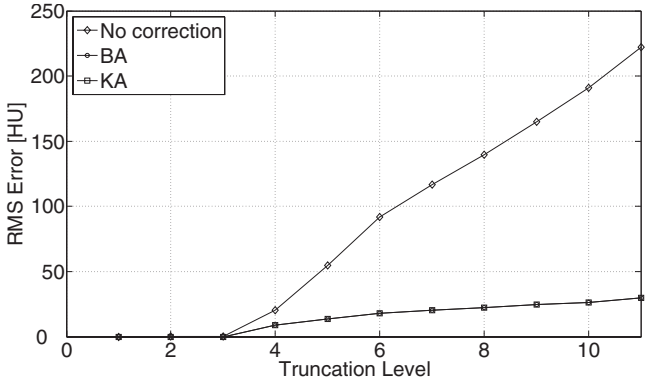

FIG. 16. The RMS error is shown for different levels of trans-axial data truncation. The curve with diamonds shows the case without truncation correction. The curve with circles shows the case when applying the basic approach and the curve with squares when applying the kink approach. However, these last two curves are very similar and cannot be distinguished from each other on the plot.

In the trans-axial data truncation experiment of Fig. 16, we can first look at the curve where no truncation correction was applied (the curve with diamonds). In this case, we see that the RMS error rises constantly, starting from truncation level 3 until it finally reaches a value of 222 HU. In contrast, the BA curve (the curve with circles) and the KA curve (the curve with squares) rise at a much lower RMS error level. Both BA and KA curves reach a final value of 29 HU. This corresponds to a difference of 193 HU compared to the curve where no truncation correction was applied. Because BA and KA share the same implementation when it comes to trans-axial data truncation, both curves are identical.

For the axial data truncation experiment in Fig. 17, we again consider first the curve where no truncation correction was applied (the curve with diamonds). This curve rises until truncation level 8, where it starts to fall again until it finally reaches a value of 21 HU at truncation level 11. This curve behavior may be explained by the fact that those parts of the object which have a strong contribution to the RMS error fall outside the scan field of view beyond truncation level 8 and are thus not considered in the computation of the RMS error.

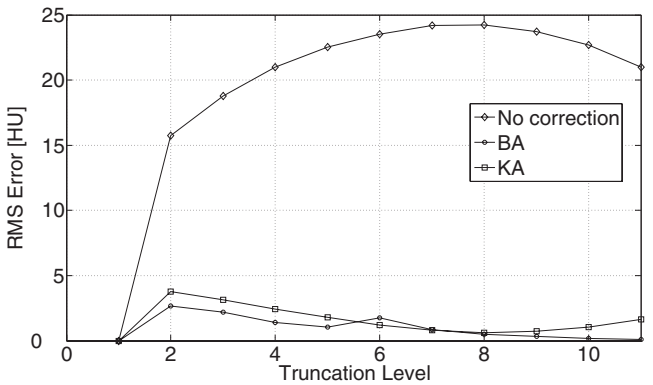

FIG. 17. The RMS error is shown for different levels of axial data truncation. The curve with diamonds shows the case without truncation correction. The curve with circles shows the case when applying the basic approach and the curve with squares when applying the kink approach.

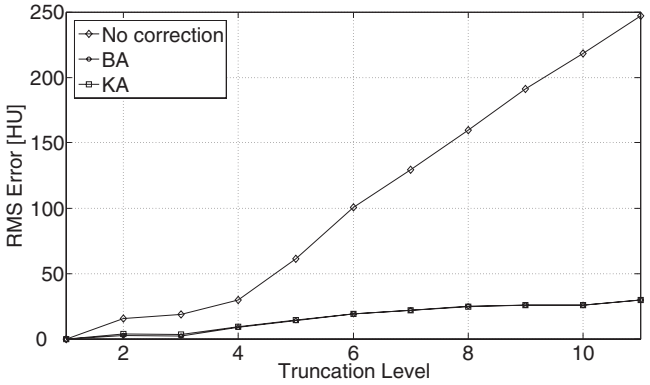

FIG. 18. The RMS error is shown for different levels of combined data truncation. The curve with diamonds shows the case without truncation correction. The curve with circles shows the case when using the basic approach and the curve with squares when using the kink approach. However, these last two curves are very similar and cannot be distinguished from each other on the plot.

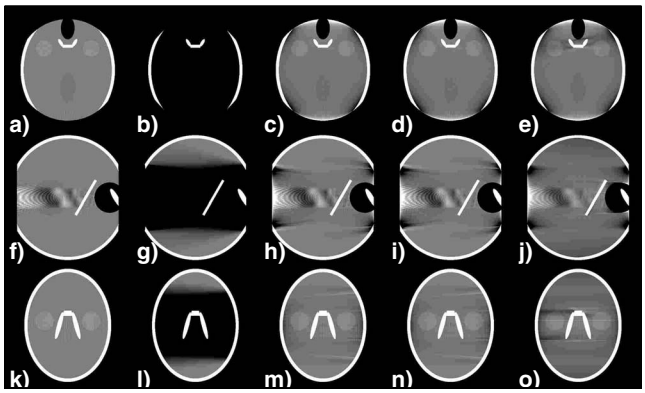

FIG. 19. Reconstruction of three slices at $z=20$ mm, $y=50$ mm, and $x=0$ mm (from top to bottom) through the FORBILD head phantom for trans-axial data truncation. In (a), (f), (k), the ground truth, in (b), (g), (l), the reconstruction without truncation correction, in (c), (h), (m), the reconstruction using the basic approach, in (d), (i), (n), the reconstruction using the kink approach, and in (e), (j), (o), the FDK reconstruction using the hybrid approach is shown. The window was set to [−30 HU; 130 HU].

Of course this behavior depends on the chosen phantom as well as on the chosen geometrical setup. For the BA curve (the curve with circles) and the KA curve (the curve with squares), we see that with the exception of truncation level 6, the RMS error of the basic approach is always slightly lower than that of the kink approach. The BA curve finally reaches a value of 0.1 HU while the KA curve reaches a value of 1.6 HU at truncation level 11. In any case, comparing Figs. 16 and 17, we observe that axial data truncation is a much less severe problem than trans-axial data truncation.

For the combined data truncation experiment in Fig. 18, the curve progressions mostly emulate the trans-axial data truncation case (except for the truncation levels 2 and 3) since, in this combination, the errors caused by trans-axial data truncation are higher than those caused by axial data truncation.

IV.E. Visual image quality

In this section, we compare the reconstructed images by visual inspection rather than by quantitative analysis. For each experiment, we picked the images with the maximal DoT values, corresponding to the highest truncation level. We show the ground truth reconstruction and a reconstruction without truncation correction along with reconstructions using the basic approach and the kink approach. We also show FDK reconstructions, where we applied the hybrid approach along the detector rows for truncation correction; this amounts to applying step BA-R on the truncated data. The FDK results allow us to compare the performance of the FDK algorithm with the original hybrid approach to the M-line algorithm with our proposed methods.

For this visual inspection, we chose three orthogonal slices through the FORBILD head phantom. The slices were at $z=20$ mm, $y=50$ mm, and $x=0$ mm. The results for trans-axial, axial, and combined data truncation can be seen in Figs. 19–21, respectively.

From Fig. 19, we see an extreme intensity drop-off when no truncation correction is applied. The intensity drop-off manifests as almost uniformly black shadows due to the chosen gray window, in those regions where the filtering lines are truncated. The basic approach and the kink approach restore the image such that all high and low contrast inlays can be clearly identified. The methods are not able to resolve the data truncation problem without remaining artifacts. Those artifacts appear as small located black shadows and as directed nonlocated streaks throughout the volume. In those regions, the assumptions of the underlying water cylinder correction seem to be too weak. However, both methods clearly outperform the case without truncation correction.

Figure 20 shows the same intensity drop-offs when no truncation correction is applied. In contrast to the trans-axial data truncation scenario, those shadows cover a much smaller portion of the object. However, the artifacts are severe enough to mask important details of the FORBILD head phantom. The shape and location of the shadows are a con-

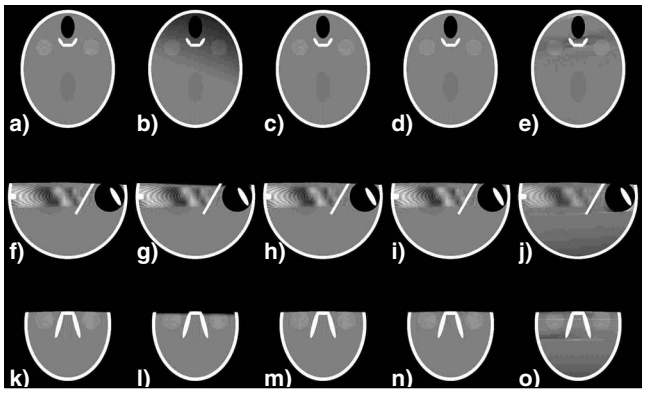

FIG. 20. Reconstruction of three slices at $z=20$ mm, $y=50$ mm, and $x=0$ mm (from top to bottom) through the FORBILD head phantom for axial data truncation. In (a), (f), (k), the ground truth, in (b), (g), (l), the reconstruction without truncation correction, in (c), (h), (m), the reconstruction using the basic approach, in (d), (i), (n), the reconstruction using the kink approach, and in (e), (j), (o), the FDK reconstruction using the hybrid approach is shown. The window was set to [−30 HU; 130 HU].

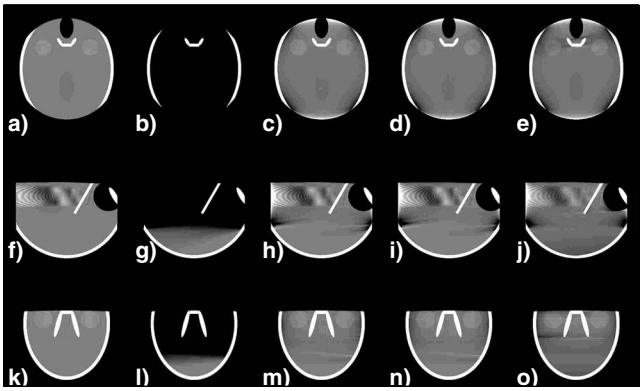

FIG. 21. Reconstruction of three slices at $z=20$ mm, $y=50$ mm, and $x=0$ mm (from top to bottom) through the FORBILD head phantom for combined data truncation. In (a), (f), (k), the ground truth, in (b), (g), (l), the reconstruction without truncation correction, in (c), (h), (m), the reconstruction using the basic approach, in (d), (i), (n), the reconstruction using the kink approach, and in (e), (j), (o), the FDK reconstruction using the hybrid approach is shown. The window was set to [−30 HU; 130 HU].

sequence of the chosen experimental setup (M-point location, geometry, etc.). For axial data truncation, both basic approach and kink approach recover the object almost perfectly. No differences in visual image quality can be seen between the two truncation correction methods.

Without truncation correction in Fig. 21, the outcome appears almost identical to the trans-axial truncation case since these artifacts are dominant. However, in fact, the artifacts are composed of trans-axial and axial data truncation. The basic approach and the kink approach show small located shadows and directed nonlocated streaks as expected from the trans-axial data truncation case but otherwise restore the images quite well.

Figure 22 shows the results of combined data truncation from one realization of Poisson noise (250 000 photons). From the figure, we observe that both the basic approach and the kink approach seem to be robust to noise, at least for this particular data set. The outcome seems to be analog to that of Fig. 21.

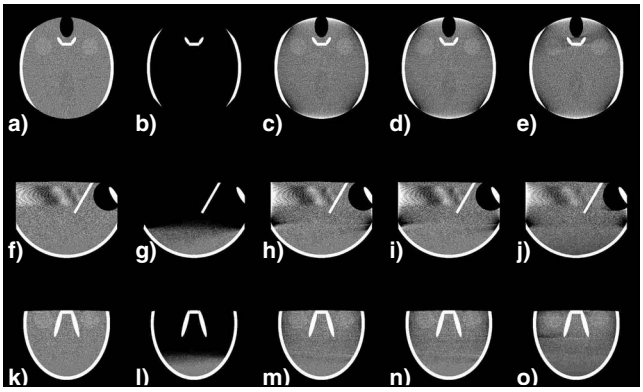

FIG. 22. Reconstruction of three slices at $z=20$ mm, $y=50$ mm, and $x=0$ mm (from top to bottom) through the FORBILD head phantom for combined data truncation from one realization of Poisson noise (250 000 photons). In (a), (f), (k), the ground truth, in (b), (g), (l), the reconstruction without truncation correction, in (c), (h), (m), the reconstruction using the basic approach, in (d), (i), (n), the reconstruction using the kink approach, and in (e), (j), (o), the FDK reconstruction using the hybrid approach is shown. The window was set to [−30 HU; 130 HU].

V. CONCLUSIONS

We have presented two empirical methods to handle data truncation for oblique filtering lines. Both methods are based upon the so-called hybrid approach, which is a truncation correction technique for horizontal filtering lines that is applied to the FDK algorithm. The basic approach compensates data truncation in two successive preprocessing steps. It is therefore independent of any specific reconstruction algorithm. The kink approach uses similar concepts for data extrapolation as the basic approach but adapts the filtering lines when necessary. It therefore needs to be integrated into the reconstruction algorithm. In both methods, truncation correction is done solely for the purpose of filtering. No extrapolated value is ever backprojected.

The methods were tested on simulated data of the FORBILD head phantom. The results show that truncation effects resulting from oblique lines can be considerably mitigated. Unfortunately, some artifacts remain, especially in the case of trans-axial data truncation (truncation along the detector rows). These artifacts appear in the form of small intensity drops in the vicinity of truncated edges, and in the form of low-intensity streaks that radiate from these edges and spread over the entire reconstructed volume. We note that they were already present in the FDK reconstruction, but they were then less noticeable because of the numerous CB artifacts that mask them.

Since the streaks and intensity drops are present in both the FDK reconstruction and the M-line reconstruction, we may assume that they are caused by the hybrid approach itself. Using the empirical hybrid approach to handle oblique filtering as suggested in the basic approach and the kink approach does not seem to generate additional types of artifacts. Refinements of the hybrid approach aiming at reducing these artifacts are beyond the scope of this paper, but will be investigated in the future.

Our quantitative analysis highlighted only small differences between the basic approach and the kink approach, and these differences lead to no visual differences between the noise-free reconstructions achieved with these two methods. Also, addition of noise did not change this observation. Both methods appear equally robust to noise, and we believe that this feature is a direct attribute of the robustness of the hybrid approach, on which both methods are built. Consequently, preference for one method versus the other should be primarily based on ease of implementation and specifics of the data acquisition geometry. As mentioned earlier, the kink approach offers a gain in data storage, but is also not applicable to all data acquisition geometries.

In our experiments and in the presented drawings, the M-point projected always outside of the detector. This will always be the case, if the M-point is chosen to be approximately in the middle of the partial-circle segment of the partial-circle-plus-arc trajectory, at least for a realistic C-arm

geometry, e.g., see Ref. 13. In general, no severe consequences are to be expected if the M-point projects inside of the detector. Both methods may still be applied without changes. However, if the M-point projects onto the back-projection region itself, some of the resulting filtering lines will become vertical, e.g., they will have the same orientation as the detector columns. For those filtering lines, the kink approach cannot be applied as presented, since in the case of axial data truncation, the method would infinitely repeat the last projection value whenever a (vertical) filtering line leaves the detector. The basic approach does not have this specific problem and should be thus preferred in that case.

Our methods can be applied, besides the M-line approach, to any FBP algorithm that requires oblique filtering lines, e.g., the Katsevich partial-circle-plus-line[15] or partial-circle-plus-arc[4] algorithms or the ACE algorithm.[3]

ACKNOWLEDGMENTS

This work was supported by Siemens AG, Medical Solutions and was supported in part by the U.S. National Institutes of Health (NIH) under Grant No. R01 EB000627. Disclaimer: The concepts and information presented in this paper are based on research and are not commercially available.

[a]Electronic mail: hoppe@informatik.uni-erlangen.de
[b]Electronic mail: joachim.hornegger@informatik.uni-erlangen.de
[c]Electronic mail: guenter.lauritsch@siemens.com
[d]Formerly with UCAIR, Department of Radiology, University of Utah, UT. Electronic mail: frank.dennerlein@siemens.com
[e]Electronic mail: noo@ucair.med.utah.edu

[1]X. Wang and R. Ning, "A cone beam reconstruction algorithm for circle-plus-arc data-acquisition geometry," IEEE Trans. Med. Imaging **18**, 815–824 (1999).
[2]L. A. Feldkamp, L. C. Davis, and J. W. Kress, "Practical cone-beam algorithm," J. Opt. Soc. Am. A **1**, 612–619 (1984).
[3]B. E. Nett, T. Zhuang, and G.-H. Chen, "A cone-beam FBP reconstruction algorithm for short-scan and super-short-scan source trajectories," Fully 3D Image Reconstruction in Radiology and Nuclear Medicine, Salt Lake City, UT, 6–9 July 2005, pp. 396–400.
[4]A. Katsevich, "Image reconstruction for the circle-and-arc trajectory," Phys. Med. Biol. **50**, 2249–2265 (2005).
[5]J. Pack and F. Noo, "Cone-beam reconstruction using 1D filtering along the projection of M-lines," Inverse Probl. **21**, 1105–1120 (2005).
[6]G. Wang, Y. Liu, T. H. Lin, and P. C. Cheng, "Half-scan cone-beam x-ray microtomography formula," Scan Electron Microsc. **16**, 216–220 (1994).
[7]B. Ohnesorge, T. Flor, K. Schwarz, J. P. Heiken, and K. T. Bae, "Efficient correction for CT image artifacts caused by objects extending outside the scan field of view," Med. Phys. **27**, 39–46 (2000).
[8]K. J. Ruchala, G. H. Olivera, J. M. Kapatoes, P. J. Reckwerdt, and T. R. Mackie, "Methods for improving limited field-of-view radiotherapy reconstructions using imperfect a priori images," Med. Phys. **29**, 2590–2605 (2002).
[9]J. Hsieh, E. Chao, J. Thibault, B. Grekowicz, A. Horst, S. McOlash, and T. J. Myers, "A novel reconstruction algorithm to extend the CT scan field-of-view," Med. Phys. **31**, 2385–2391 (2004).
[10]M. Zellerhoff, B. Scholz, E.-P. Rührnschopf, and T. Brunner, "Low contrast 3D-reconstruction from C-arm data," Proc. SPIE **5745**, 646–655 (2005).
[11]A. A. Zamyatin and S. Nakanishi, "Extension of the reconstruction field of view and truncation correction using sinogram decomposition," Med. Phys. **34**, 1593–1604 (2007).
[12]H. K. Tuy, "An inversion formula for cone-beam reconstruction," SIAM J. Appl. Math. **43**, 546–552 (1983).
[13]S. Hoppe, F. Dennerlein, G. Lauritsch, J. Hornegger, and F. Noo, "Cone-beam tomography from short-scan circle-plus-arc data measured on a C-arm system," IEEE Nuclear Science Symposium Conference Record, (2006), Vol. 6, pp. 2873–2877.
[14]M. Kachelrieß, M. Knaup, and W. A. Kalender, "Extended parallel back-projection for standard three-dimensional and phase-correlated four-dimensional axial and spiral cone-beam CT with arbitrary pitch, arbitrary cone-angle, and 100% dose usage," Med. Phys. **31**, 1623–1641 (2004).
[15]A. Katsevich, "Image reconstruction for the circle-and-line trajectory," Phys. Med. Biol. **49**, 5059–5072 (2004).